



The role of the Indian Ocean Dipole in modulating the Austral Spring ENSO teleconnection into the Southern Hemisphere.

Luciano G. Andrian^{1,2,3}, Marisol Osman^{1,2,3}, and Carolina S. Vera^{1,2,3}

¹Departamento de Ciencias de la Atmósfera y los Océanos, Facultad de Ciencias Exactas y Naturales, Universidad de Buenos Aires, Buenos Aires, Argentina.

²CONICET-Universidad de Buenos Aires, Centro de Investigaciones del Mar y la Atmósfera (CIMA), Buenos Aires, Argentina.

³CNRS-IRD-CONICET-UBA, Instituto Franco-Argentino para el Estudio del Clima y sus Impactos (IRL3351 IFAECI), Buenos Aires, Argentina

Correspondence: Luciano G. Andrian (luciano.andrian@cima.fcen.uba.ar)

Abstract. The combined influence of El Niño-Southern Oscillation (ENSO) and the Indian Ocean Dipole (IOD) on the extratropical circulation in the Southern Hemisphere (SH) during austral spring is examined. Reanalyses and the large ensemble of CFSv2 model outputs, were used to compute composites and linear regressions for relevant variables. The results show that positive IOD can reinforce the El Niño-induced circulation by merging the Indian Ocean wave train with the PSA-like pattern over the Pacific Ocean. In addition, the results obtained with the CFSv2 model output shows that strong positive IODs can contribute to enhancing the circulation signal of the El Niño anomalies and the Indian Ocean wave train. On the other hand, negative IODs in combination with La Niña do not have that combined circulation response. While there is a moderate intensification of the circulation anomalies associated with La Niña, accompanied by some changes in the location of their main action centers, results vary considerably between linear regression, the observed and model composites. Regarding the influence of the IOD activity (independent of ENSO), reanalysis-based results show that the IOD positive phase has a significant impact over the entire SH, while the negative phase is associated with weaker anomalies and a large inter-event variability.

1 Introduction

In recent decades, significant advancements have been made in the scientific community regarding our understanding of the effects of the El Niño-Southern Oscillation (ENSO), spanning from large-scale circulation to its effects in various parts of the world. Nevertheless, ENSO is not the exclusive mode of oceanic variability in the tropical region; each basin displays its own independent variability that can interact with the others. One of the most common combinations with ENSO is the Indian Ocean Dipole (IOD). The dynamics, feedbacks, and effects of ENSO-IOD interactions have been extensively studied in tropical regions, particularly those adjacent to the Indian Ocean (IO) (Vinayachandran et al., 2010; Zhao et al., 2019; Wang et al., 2019). Similarly, the inquiry into whether IOD operates independently of ENSO has been significant since the discovery of IOD, and it remains an open question (Sun et al., 2015; Fan et al., 2016; Stuecker et al., 2017). However, the modulation of teleconnections in extratropical latitudes of the Southern Hemisphere (SH) by ENSO and IOD has received less attention.



The ENSO exerts its influence on the middle and high latitudes of the SH through equivalent barotropic Rossby wave train, which emerge in response to the anomalous convection in the tropical Pacific and propagates from there, veering towards South America. This wave train is typically referred to as the Pacific South American patterns (PSA, Karoly, 1989; Mo, 2000) and is the second dominant mode of variability in the SH, after the Southern Annular Mode (SAM). The third mode of variability, commonly referred to as PSA2, is linked to quasi-biennial variations of ENSO and is associated with SST variations in the tropical IO (Mo, 2000).

The IOD (Saji et al., 1999) is a mode of variability characterized by a dipole of east-west SST anomalies in the IO. Its activity peaks during austral winter and spring influencing climate on seasonal scales in the vicinity of the IO. Also, this dipole of SST anomalies can alter the tropical convection, causing remote effects through teleconnections. Previous research has shown that the IOD can induce large-scale circulation anomalies in the SH through wave trains propagating from the IO through the middle and high latitudes of the Pacific Ocean, reaching even South America (Saji and Yamagata, 2003b; Saji et al., 2005; Chan et al., 2008; Cai et al., 2011). Moreover, many of these works assumed a linear response between the IOD phases, where the magnitude of the response is equal but with opposite signs. This assumption led to the generalization of IOD effects based solely on composites of positive events only, without showing those of negative events (Saji and Yamagata, 2003b; Saji et al., 2005). However, such symmetry in the magnitude of the response between the two IOD phases does not seem to hold true for climate impacts beyond the IO region. For instance, Chan et al. (2008) noted that the response of the negative phase of the IOD on precipitation in South America is less consistent compared to the positive phase. Similarly, Cai et al. (2011) initially concluded the existence of symmetry in the intensity response of both phases of the IOD based on partial linear regression, but subsequent analysis by Cai et al. (2012) using linear regression demonstrated the asymmetry in the phases of the IOD and their associated teleconnections. In particular, they found a stronger signal in circulation anomalies for positive IOD events than for the negative ones.

Atmosphere-ocean dynamics make the anomalous SST pattern of positive IOD events more intense than the negative ones (Cai et al., 2013). In addition, other seasonally dependent dynamical processes may affect the propagation of wave trains associated with each IOD phase. Through model experiments, Gillett et al. (2022) showed for the austral winter how negative IOD events promote wave trains toward extratropical latitudes, despite the barrier imposed by the negative meridional gradient of mean absolute vorticity associated with the polar flank of the subtropical jet. They also found that the atmospheric response in the equatorial IO for negative IOD events is larger than that for the positive ones. However, Sena and Magnusdottir (2021) found quite similar wave trains over the south Pacific ocean associated with both phases of the IOD in the austral spring also through modeling studies.

Previous works have identified a relationship between ENSO and the IOD through a positive and significant correlation between the Dipole Mode Index and Niño 3.4 index. Moreover, at extratropical latitudes, Cai et al. (2011) found that in the austral spring (defined as September-October-November (SON)) both poles of the IOD (located on the eastern and western sides of the IO basin) seems to promote the development of two separated wave trains that converge south of Australia and subsequently merge with the PSA pattern induced by ENSO in the subtropical central Pacific. However, due to the high correlation observed between both indices and the methodology of partial linear regression, the authors conclude that it is not



possible to completely isolate the effects of the IOD and ENSO in that particular season. Later, Cai et al. (2012) using linear regression demonstrated that the combination of El Niño and positive IOD exhibits a stronger impact on the extratropical circulation compared to the combination of a negative IOD and La Niña, particularly over the IO. These studies reveal that different approaches to the subject can lead to varying results, hence giving rise to considerable uncertainty.

The aims of this study is to increase our understanding of the influence of the IOD on the extratropical circulation of the SH including the IOD modulation of the ENSO-extratropical teleconnection. The focus of the study is in the extratropics and thus we do not address the dynamics of the combined ENSO-IOD activity in the tropical region, nor do we discuss the dependence between both climate variability patterns. The paper is organized as follows: Section 2 describes the data and methodology used, Section 3 presents the main results and Section 4 discusses the main conclusions.

2 Data and Methodology

We focused on the period 1940-2020 and in the austral spring, defined by the quarter SON, when both ENSO and IOD have the greatest influence on the SH. The NOAA Extended Reconstructed SST V5 (ERSSTv5, Huang et al., 2017) was used to identify and categorize ENSO and IOD events. Data on divergence and velocity potential at 200hPa, and geopotential height at 750hPa and 200hPa, were obtained from the ECMWF ERA5 reanalysis (Hersbach et al., 2020) to characterize the circulation conditions. Precipitation and temperature anomalies were described using the Global Precipitation Climatology Centre v2020 (GPCC. Schneider et al., 2020) dataset at $0.25^\circ \times 0.25^\circ$ resolution and from the gridded Climatic Research Unit (CRU) Time-series (TS) data version 4.05 (Harris et al., 2020), respectively. The linear trend was filtered, and a 3-month seasonal mean was calculated for all variables. It is noteworthy that the conclusions of this study do not change substantially if the period is limited to the satellite era (not shown).

The Niño 3.4 Index and the ENSO events were obtained following the Climate Prediction Center (https://origin.cpc.ncep.noaa.gov/products/analysis_monitoring/ensostuff/ONI_v5.php). The Dipole Mode Index (DMI, Saji and Yamagata, 2003a) was used to identify and categorize IOD events. This index describes the zonal gradient of SST anomalies in the IO through the difference between the average of these anomalies between western (IOW, 10°S - 10°N ; 50°E - 70°E) and eastern (IOE, 0°S - 10° ; 90°E - 110°E) sectors of the IO. Before computing the DMI index, the monthly anomalies of the time series for IOW and IOE were calculated based on the 1940-2020 climatology, filtering out the linear trend and interdecadal anomalies defined as periodicities longer than 7 years, and applying a 3-month running mean. Unlike Saji and Yamagata (2003a), we did not filter out the lagged effect of ENSO on tropical IO SST anomalies. We define an IOD event when the magnitude of the DMI exceeds half of its standard deviation (SD) in the average quarterly SON of each year.

Previous studies that relied solely on the composite technique to analyze the atmospheric effects of IOD (Saji and Yamagata, 2003b; Saji et al., 2005) face a constraint in the robustness of their results due to the small size of the observed samples. This limitation also applies to the ENSO response in cases of pure events, i.e., without IOD. Therefore, we also used a large ensemble of initialized predictions from the CFSv2 model (Saha et al., 2014) to address the impact of sampling uncertainty and to allow the detection of nonlinearities in the response to each forcing. We used SST and z200 forecasts for SON (3-month



90 seasonal mean) initialized 0, 1, 2, and 3 months in advance, i.e., from June to September, in the period combining hindcast
(1982-2011) with real-time forecasts (2011-2020). Since the CFSv2 model has 24 ensemble members, the total sample has
approximately 3744 ensemble members for SON. SON anomalies were calculated based on different periods due to the abrupt
shift in the climatology of the CFSv2 SST forecasts between 1998 and 1999 (Kumar et al., 2012; Saha et al., 2014). Following
Kumar and Chen (2017), for the period 1982-1998, the seasonal anomalies are based on the climatology of the same period,
95 and for 1999-2020 are based on the climatology of 1999-2011. The linear trend of the anomalies were filtered separately for
the periods 1982-1998, 1999-2011, and 2011-2020. In the CFSv2 model, the DMI and Niño 3.4 indices were computed from
the seasonal mean of the SST anomalies in SON for each forecast in the sample. For the simulation a IOD or ENSO event is
defined when the index magnitude exceeds $0.5 \cdot SD$ of each index over the entire sample.

To isolate the influence on the atmospheric anomalies of ENSO and IOD that are linearly independent of each other, we
100 used the partial regression technique, following Cai et al. (2011). This technique consists of computing the linear regression
between a predictand (e.g., z_{200}) and a predictor (e.g., Niño 3.4 index) after removing, by regression, the linear relationship
of a second predictor (e.g., DMI index) from both the predictand and the first predictor. Following the notation of Cai et al.
(2011), we will refer to this regression as the Niño 3.4_{|DMI}. Likewise the regression between a variable and DMI without the
effect of Niño 3.4 as DMI_{|Niño 3.4}. The statistical significance of the regression coefficients was estimated based on that of the
105 corresponding correlation coefficients using a t-student test at a 95% confidence level. It is important to note that due to the high
correlation between DMI and Niño 3.4, it is possible that by removing the effect of one on the other through linear regression,
some intrinsic properties of each one are also removed. Moreover, this technique is limited to capturing only the linear aspects
of the phenomenon. For ease of visual comparison, the size of the regression anomalies has been scaled by one SD anomaly of
the predictor in each case.

110 Composite fields of all variables were made by the difference between the mean of all fields in the sample (observational
or model data) with the same type of event (e.g., El Niño or positive IOD event) and the mean of all neutral fields in the
sample in which no ENSO or IOD events occurred. The significance of the observed composites was analyzed using the Monte
Carlo technique, following Osman and Vera (2017). This technique consists in computing anomaly composites by randomly
selecting N instances from a dataset of neutral events and N events of the same type (e.g., El Niño). This procedure is repeated
115 10000 times to compute the 5th and 95th percentiles of the mean anomaly composites based on 10000 values for each grid
point. Then, each anomaly composite is tested against the 5th and 95th percentiles to assess its significance. We divide the
composites into 3 cases, ENSO pure, IOD pure, and simultaneous. A pure event is one in which only one, ENSO or IOD,
occurs (according to criteria explained above), and a simultaneous event is one in which both events occur simultaneously.

The robustness of the composite based on CFSv2 model predictions, was assessed by estimating the signal-to-noise ratio
120 (SNR) from each composite and for each case (e.g., El Niño), following Kumar and Chen (2017). The signal is the composite
mean, and the noise is the SD between the forecasts that make up the composite.

The wave activity fluxes, where calculated to describe the energy dispersion associated with the teleconnections, following
Takaya and Nakamura (2001).



3 Results

125 3.1 Reanalysis

Figure 1 shows the joint distribution of the Niño 3.4 and DMI indices in SON for the observed period 1940-2020. As expected, the correlation between ENSO and IOD is high (0.54), in agreement with previous works (Cai et al., 2011), and most events occur simultaneously and in the same phase, that is El Niño–positive IOD or La Niña–negative IOD. It is noteworthy that we only found two instances with events of opposite sign, characterized by positive IOD and La Niña, and negative IOD and El Niño. In addition, only a few pure events were identified to analyze the individual response without resorting to any filtering technique, such as partial regression. Moreover, as reported in previous works, it is evident that pure positive IOD events have a larger magnitude than pure negative ones.

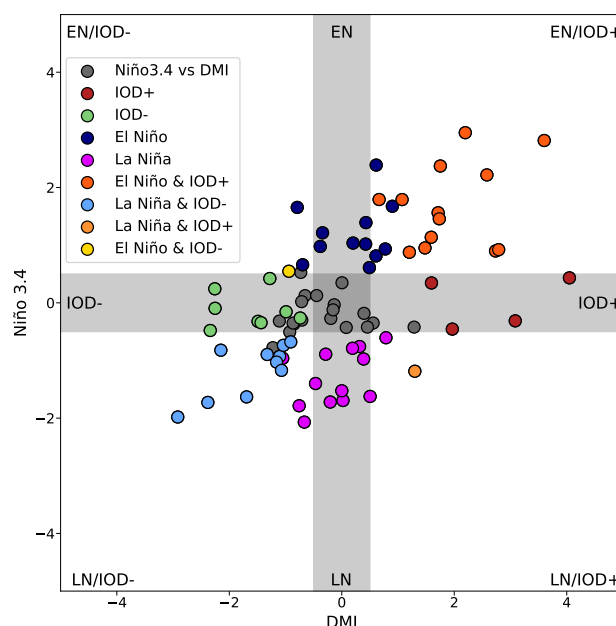


Figure 1. Scatter plot between the DMI and Niño 3.4 indices in SON for 1940-2020. The blue (magenta) and dark red (green) colors denote pure El Niño (La Niña) and positive (negative) IOD events, respectively. Simultaneous positive (negative) events are shown in red (light blue). The horizontal and vertical gray bands indicate the threshold for determining the events (see text).

The regression fields for the anomalies of SST, divergence, and velocity potential at 200 hPa associated with Niño 3.4, $Ni\tilde{n}o_{3.4}|_{DMI}$, DMI and $DMI|_{Ni\tilde{n}o_{3.4}}$ in SON are shown in Fig. 2. The full regression fields for ENSO and IOD (Fig. 2a and b, respectively) are very similar due to the high correlation between their indices. However, the SST anomalies in the equatorial Pacific are larger in the Niño 3.4 than for DMI. Moreover, the Walker circulation is also stronger for Niño 3.4, as shown by regions of divergence (upward motion) in the equatorial Pacific and convergence (downward motion) over the maritime continent and eastern IO. For IOD (Fig. 2b), the Walker circulation is weaker and the upward motion over the western IO and



east Africa associated with the convection due to the warm SST is more evident than for ENSO. The Niño 3.4|_{DMI} regression
140 field (Fig. 2c) shows a small signal of ENSO on the SST anomalies in the IO. Moreover, the downward branch of the Walker
circulation over the maritime continent and the eastern IO is more widespread and less intense than for Niño 3.4 full regression.
On the other hand, the DMI|_{Niño3.4} regression pattern (Fig. 2d) shows almost no connection between the IOD and the anomalies
of both SST and the atmospheric circulation in the Pacific Ocean. The Walker circulation is weaker compared to the full
regression and is restricted to the IO basin.

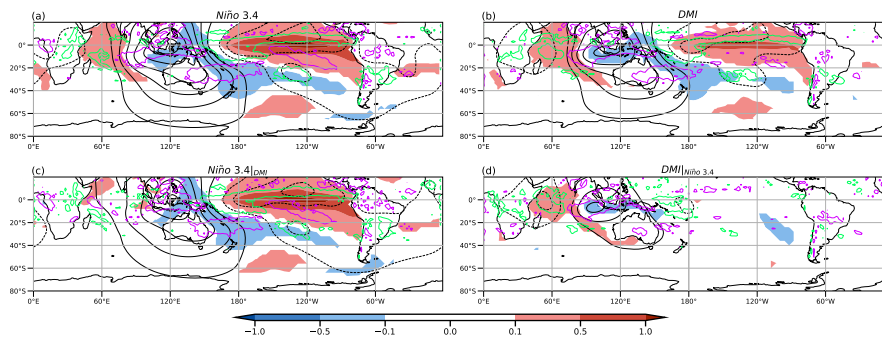


Figure 2. Regression of SST anomalies ($^{\circ}\text{C}$, shaded), velocity potential (black contours by $0.5 \times 10^6 \text{ m}^2 \text{ s}^{-1}$), and significant divergence based on a 95% t-student test (colored contours at $-5 \times 10^{-6} \text{ s}^{-1}$ and $5 \times 10^{-6} \text{ s}^{-1}$) at 200hPa on Niño 3.4(a), DMI (b), partial Niño 3.4 (c) and partial DMI (d).

145 As for the previous variables, the z200 (Fig. 3) anomaly regression fields for ENSO and IOD are similar, but the former
has stronger anomalies. For both ENSO and IOD full regressions (Fig. 3a and b, respectively), a PSA-like pattern, across
the central Pacific, is evident as well as a wave train (IO wave train, following Cai et al. (2011)) emanating from the eastern
IO southeastward to high latitudes. However, the WAF shows that the IO wave train only contributes to the PSA-like pattern
over the South Pacific for the IOD full regression (Fig. 3b). At 750hPa circulation anomalies depict almost negligible values
150 equatorwards of 20°S for all cases (Fig. 4). The ENSO full regression for this level (Fig. 4a) shows an anticyclonic anomaly
over the IO basin with largest values to the west of Australia that links with a cyclonic anomaly in the central south Pacific
associated with the PSA-like pattern. A very similar pattern is observed in the case of the IOD full regression at 750hPa
(Fig. 4b), but this anticyclonic anomaly is located slightly further east of the IO, the Maritime Continent, and Australia, and it
is more intense than in the ENSO full regression. Unlike at the upper level, the WAF at 750hPa shows the contribution of the
155 IO wave train to the PSA-like pattern for both ENSO and IOD full regressions (Fig. 4a and b, respectively). Cai et al. (2011)
identified this wave train as equivalent barotropic and suggested that, in SON, it arises from the joint contribution of the east
and west IO convection anomalies. This results in a more zonal propagation compared to that observed in austral winter, where
only the eastern IO contributes (Cai et al., 2011).

The analysis of Niño 3.4|_{DMI} shows for z200 that IO wave train reduces its intensity and loses significance in (Fig. 3c)
160 compared to the Niño 3.4 full regression (Fig. 3a). This is consistent with the weakening of the divergence at 200hPa (cf.

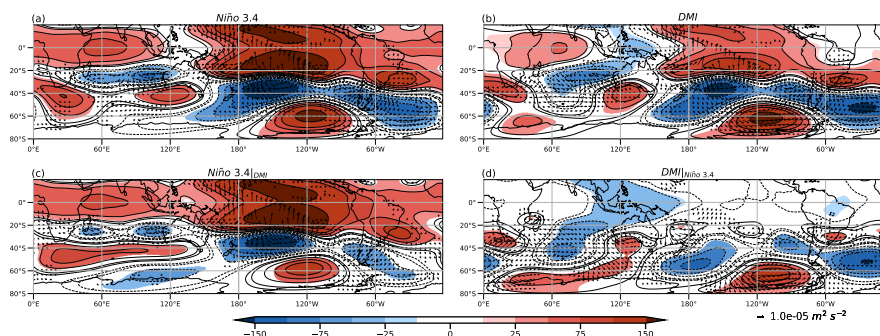


Figure 3. Regression of geopotential height (m, shaded and contours) and wave activity flux ($\text{m}^2 \text{s}^{-2}$, vectors) at 200hPa onto Niño 3.4(a), DMI (b), partial Niño 3.4 (c) and partial DMI (d). Colored regions indicate 95% statistical significance with a t-test.

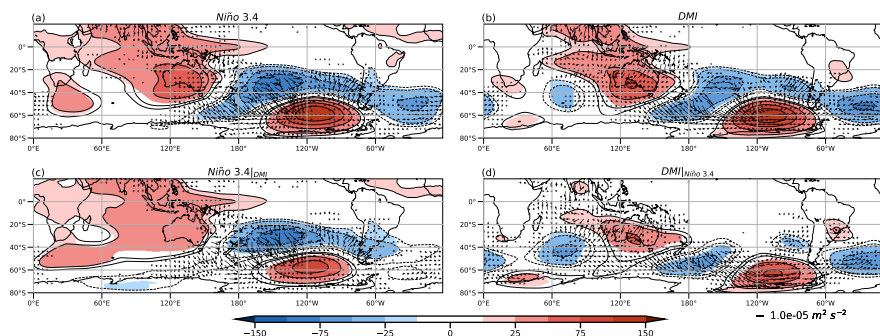


Figure 4. As in Fig. 3 but for 750hPa.

Fig. 2a and c) at eastern IO when the IOD effect is removed. Therefore, the IO wave train no longer seems to contribute to the PSA pattern, which is slightly weaker. At 750hPa the Niño 3.4_{DMI} regression (Fig. 4c) shows that both, the anticyclonic anomaly over Australia and the cyclonic anomaly downstream lose intensity, while the wave train propagation towards the Pacific Ocean, as described by the WAF, is no longer evident. On the other hand, in the DMI_{Niño3.4} regressions at both levels, the IO wave train maintains its significance with an equivalent barotropic structure and propagates throughout the high latitudes of the SH from the IO and the southern region of Australia (Fig. 3d and 4d).

These results confirm that IOD by itself can affect circulation anomalies throughout the SH at middle and high latitudes. In addition, the co-occurrence of ENSO and IOD events could lead to enhanced ENSO circulation response.

Given the limitations of the regression technique in capturing only linear aspects and its possible insufficiency in completely isolating effects due to the strong correlation between ENSO and IOD, we also explored composites for pure IOD and ENSO events separately, as well as for their combinations.

In general, the SST composites (Fig. 5) resemble the regressed anomalies in spatial distribution and sign. However, for both pure event composites, weak SST anomalies appear in the basin where the other event takes place, such as negative SST



anomalies in the equatorial Pacific region for the positive IOD composite (Fig. 5c). Concerning the composites for divergence
 175 and velocity potential at 200hPa, they also resemble the corresponding regression fields in spatial distribution and sign. How-
 ever, while the intensity of the Walker circulation is similar between both ENSO phases (Fig. 5a and b), it is much more intense
 for the positive IOD (Fig. 5c) compared to its negative phase (Fig. 5d). Accordingly, in the case of the simultaneous events, the
 Walker circulation is enhanced in El Niño–positive IOD (Fig. 5e) but not in La Niña–negative IOD (Fig. 5f).

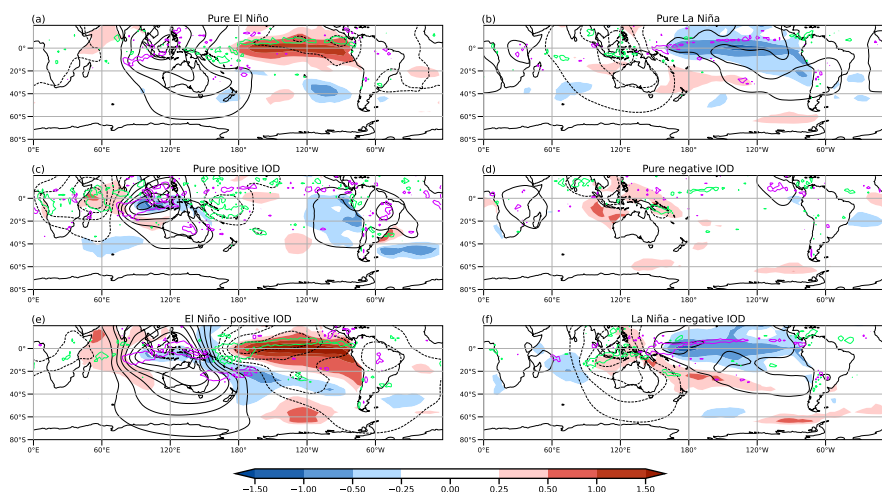


Figure 5. Composites of SST anomalies ($^{\circ}\text{C}$, shaded), velocity potential (black contours by $0.75 \times 10^6 \text{ m}^2 \text{ s}^{-1}$), and significant divergence based on a 95% t-student test (colored contours at $-1.6 \times 10^{-6} \text{ s}^{-1}$ and $1.6 \times 10^{-6} \text{ s}^{-1}$) at 200hPa for positive (left) and negative (right) events for ENSO (top), IOD (middle) and simultaneous ENSO-IOD (bottom).

Composites fields for z200 and z750 (Fig. 6 and 7, respectively) exhibit similar structures due to the equivalent barotropic
 180 nature of the anomalies. At both levels, composites show a typical PSA-like pattern for pure El Niño (Fig. 6a and 7a), which is
 less significant at middle and high latitudes than for the tropics. On the other hand, composites for positive IOD (Fig. 6c and 7c)
 show an IO wave train propagating downstream from the IO to South America that is very similar at middle and high latitudes
 to that associated with El Niño. Regardless of the differences in the significance of the anomalies, the anomalous circulation
 patterns for El Niño and the positive IOD correspond well with the regressed anomalies (Fig. 3c and d). The co-occurrence of
 185 positive IOD and El Niño events (Fig. 6e and 7e) is associated with a combination of the IO wave train and the PSA pattern,
 and larger anomalies over the South Pacific than those associated with the pure events. In addition, the WAF at 750hPa, are not
 very tidy for the pure positive IOD (Fig. 7c) but in conjunction with El Niño (Fig. 7e) clearly show for the combined events
 the energy dispersion associated with the merging of the IO wave train and the PSA pattern.

The z200 and z750 composites for La Niña (Fig. 6b and 7b) present the PSA-like pattern of opposite sign to El Niño and it
 190 is modulated at high latitudes when La Niña events occurring simultaneously with negative IOD events (Fig. 6f and 7f). In La
 Niña–negative IOD composite, the cyclonic anomaly in the South Pacific intensifies and shifts southward with respect to pure
 La Niña composite. From this cyclonic anomaly, a well organized wave train propagates toward South America. On the other

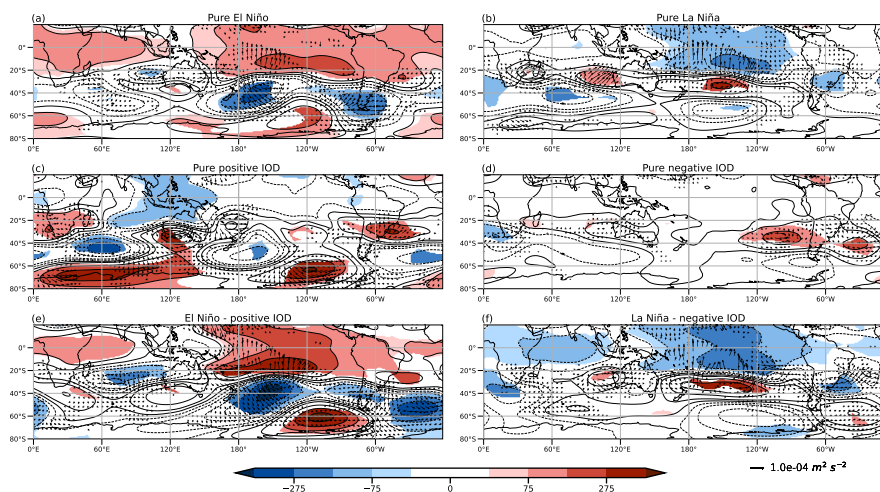


Figure 6. Composites of geopotential height anomalies (m, shaded) and wave activity flux ($m^2 s^{-2}$, vectors) at 200hPa for positive (left) and negative (right) events of ENSO (top), IOD (middle) and simultaneous ENSO-IOD (bottom). Colored regions indicate 95% statistical significance with a Monte Carlo test (see text).

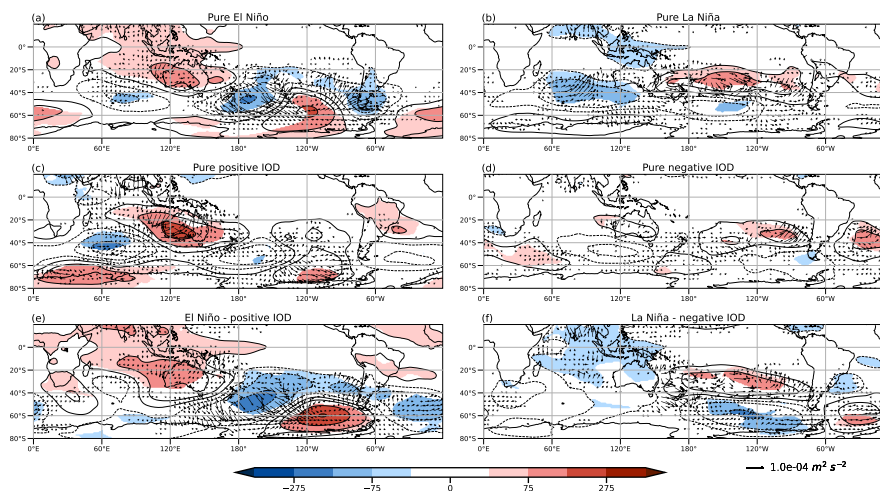


Figure 7. As 6 but for 750hPa.

hand, the negative IOD composite lacks the wave pattern observed in the positive IOD phase over the Pacific ocean. At both levels for negative IOD composite (Fig. 6d and 7d), only the mid-latitude anticyclonic anomalies are noticeable, with the most intense and significant occurring along the west coast of South America. This pattern does not resemble to the one derived from the regression (Fig. 3d).



The individual events that make up the negative IOD composite exhibit substantial variability among each other (see Fig. S1), making it challenging to identify a consistent atmospheric response when compositing. These differences may be related to the barrier created by the negative meridional gradient of mean absolute vorticity associated with the subtropical jet over southern and southwestern Australia. This area, as described through the stationary wave number K_s (Kiladis, 1998) when it is negative, hinders the propagation of the barotropic Rossby wave trains in the meridional component. According to this theoretical framework, events with a larger region of $K_s < 0$ would not exhibit clear Rossby wave patterns, while those with a smaller area of $K_s < 0$ would. While this holds true for some events, such as 1990 and 1996, it is not universally valid (see Fig. S1 and S2). Gillett et al. (2022) demonstrated for the austral winter that wave trains associated with negative IODs can propagate through this barrier by several mechanisms, which indicates that the barotropic mechanism do not dominate there. Nonetheless, the analysis of negative IOD events separately suggests that some of them encounter less favorable conditions for wave propagation, leading to more varied responses compared to the positive phase. In addition, the influence of other climate modes of variability, such as the SAM, cannot be ruled out; which can influence the propagation of Rossby waves.

These results then suggest that the positive IOD phase has a significant response in the SH circulation. In addition, the joint action of the positive IOD with El Niño tends to reinforce the typical ENSO-related circulation pattern. On the other hand, circulation anomalies for the negative IOD phase do not show the same magnitude nor consistency between individual events as for the positive phase. However, the negative IOD seems to modulate La Niña-related circulation anomalies, mainly through changes in the location and intensity of the anomalous circulation centers at middle and high latitudes that can give rise to different climate responses.

From the comparison of regressions and composites, it can be said that the magnitude of the IOD response on the large-scale circulation in the SH is not symmetric as could be assumed from the regression and as found for Cai et al. (2012). This suggests two non-exclusive hypotheses: a) forcing related to negative IOD is not intense enough to generate significant a large-scale circulation response. And b) some negative IODs events are associated with a mean state that does not favor the meridional propagation of barotropic Rossby waves at high levels, as we have just shown. This may result in a very different response in large-scale circulation between each negative event.

3.2 Model outputs

To increase the robustness of the results, we use the large ensemble from the CFSv2 model outputs described in section 2. First, we briefly assessed how the model reproduces the mean climate and the mean composites for ENSO and IOD. The Fig. S3a shows the mean differences in geopotential height at 200hPa between the model outputs and ERA5 reanalysis for SON. Overall, the model underestimates the geopotential height northward to 60°S and overestimates it southward. In addition the CFSv2 model correctly reproduces the ENSO and IOD characteristics in the SH (Fig. S3 b,c,d, e). However, over the IO the anomaly composites for both positive and negative phases of ENSO and IOD are greater than those for the reanalysis.

The joint distribution of the Niño 3.4 and DMI indices in the CFSv2 model (Fig. 8c) shows similar characteristics as the reanalysis (Fig. 1). Most of the events occur simultaneously and in the same phase and the positive IODs are more intense than the negative ones. The occurrence of El Niños alongside negative IODs and La Niñas with positive IODs is also evident



although the number of cases is less than 10% than the number of neutral events. In addition, model-based SST composites of the DMI and Niño 3.4 indices (Fig. 9) correspond to what is expected for IOD and ENSO events, respectively.

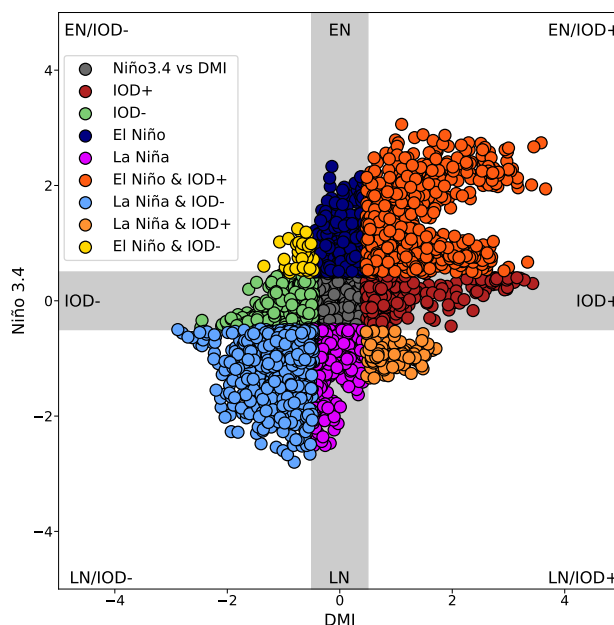


Figure 8. As Fig. 1 but for the CFSv2 model ensemble members.

We make composites following the same procedure as for the reanalysis dataset. We do not consider the composites of events in opposite phases (e.g., El Niño and negative IOD) because they represent less than 10% of the total number of neutral events.

235 For both El Niño and La Niña, the composites of z200 (Fig. 10a and b, respectively) show a PSA-like pattern, but with greater intensity for El Niño, especially at high latitudes. The positive IOD composite (Fig. 10c) closely resembles the observed ones (Fig. 6c) and the regressed (Fig. 3d) ones. Composites of simulated z200 for simultaneous positive IOD and El Niño show larger circulation anomalies through the IO wave train (Fig. 10a and e), in agreement with the observations (Fig. 6a and e). On the other hand, negative IOD composites from model outputs (Fig. 10d) resemble the regressed anomalies (Fig. 3d), but
 240 with the opposite sign. However, this pattern is totally different from the observed negative IOD composites (Fig. 6d). Negative IOD and La Niña composites describe enhanced circulation anomalies through the IO wave train (Fig. 10f). Nevertheless, the intensification of the anomalies (cf. Fig. 10a and f) at middle and high latitudes is smaller than for the simultaneous positive phase.

Figure 11 shows the signal-to-noise ratio (SNR, see Section 2) for each composite. In the El Niño and La Niña (Fig. 11a
 245 and b, respectively) composites, the SNR is higher over the tropical Pacific Ocean. However at high latitudes only in the El Niño composite the signal is comparable to the noise ($SNR \sim 0.5$). In the case of the IOD composite, for both phases the noise is larger than the signal ($SNR < 0.5$) in almost the entire SH (Fig. 11c and d). When El Niño and positive IOD occur simultaneously (Fig. 11e), the SNR intensifies its magnitude (0.7-0.8) compared to El Niño, especially in the IO wave train and

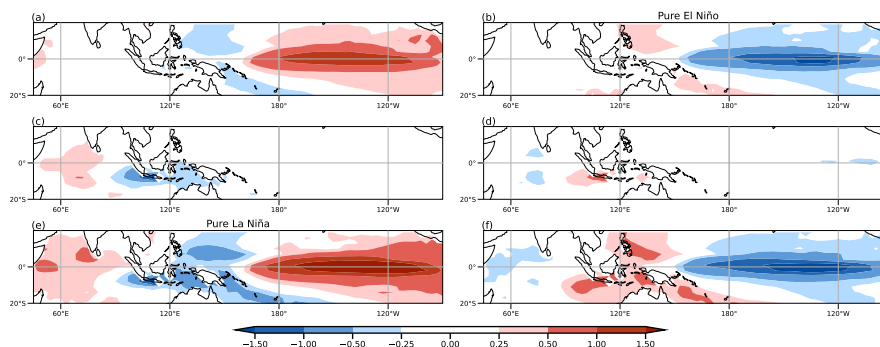


Figure 9. Composites of SST anomalies ($^{\circ}\text{C}$, shaded) from CFSv2 model for positive (left) and negative (right) events of ENSO (top), IOD (middle) and simultaneous ENSO-IOD (bottom).

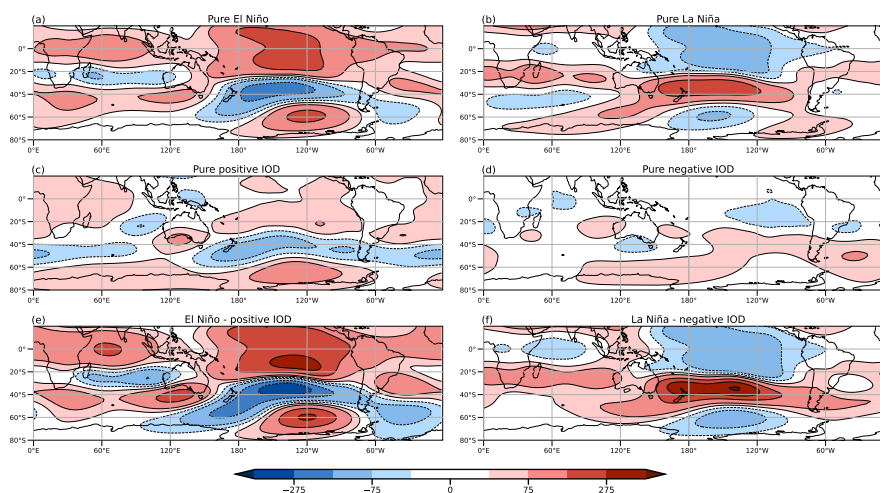


Figure 10. As 6 but for geopotential height at 200hPa.

in the PSA-like pattern at middle and high latitudes. In the case of La Niña combined with a negative IOD (Fig. 11f), the SNR values are similar to those for pure La Niña. Actually, signal enhancements in the simultaneous negative events compared to the pure La Niña are only identified over the southern IO and the South Pacific, where noise still dominates.

So far, the model results agree with the reanalysis for the positive IOD and for its joint action with El Niño. On the other hand, for negative IODs, the CFSv2 results suggest that the sample used in the observed composites may not be representative of the nature of these events. The combined action of La Niña with negative IOD seems to give rise in the model outputs to a more intense anomalous circulation than in the pure La Niña events, although it is not as strong as in the positive phase. The differences between the model results and those of the observations for La Niña and negative IOD composites could be related to the characteristics of negative IOD cases in the observational record, which are less intense than those from the model. To

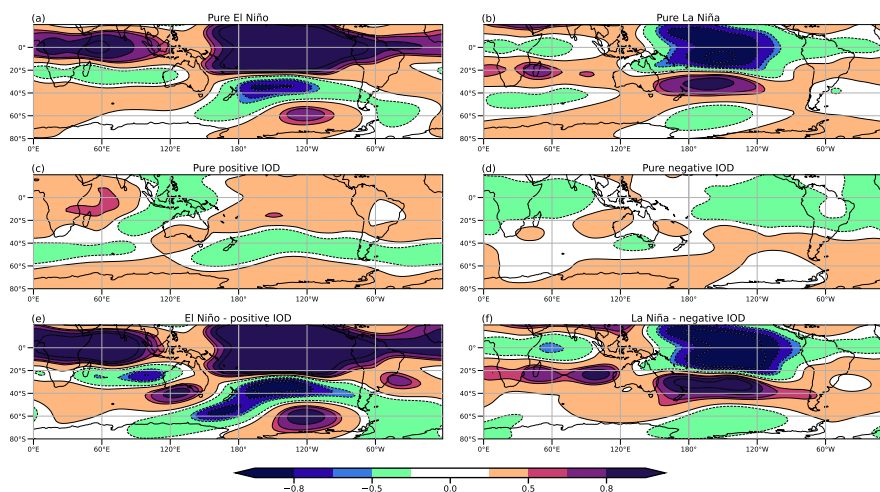


Figure 11. As 10 but for signal-to-noise ratio of geopotential height anomalies at 200hPa.

address this issue, we exploit the large ensemble to analyze the role of ENSO and IOD magnitude on the composites. Figure 12 shows the composites of the different ENSO and IOD phases conditioned on their magnitude. Using the criteria described in section 2, ENSO and IOD events were categorized into two types: moderate events (those whose magnitude was less than one standard deviation) and strong events (those whose magnitude exceeded this threshold). In agreement to the observed composites and regressions, the IO wave train is more evident in the pure positive IODs than in the pure negative ones for both moderate and strong events (middle row). In strong positive IODs, circulation anomalies are notably more intense than those in moderate events.

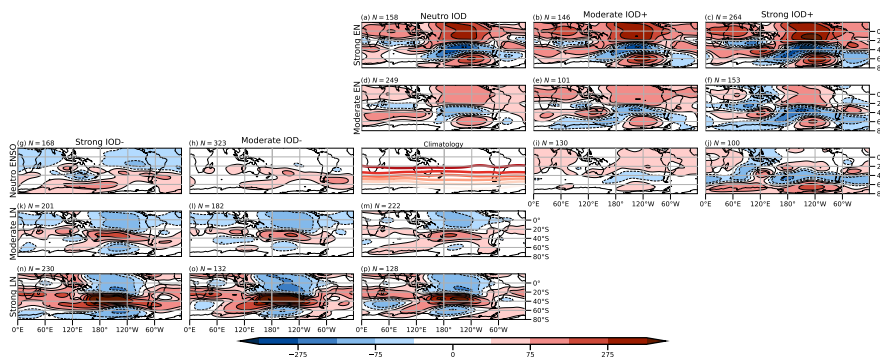


Figure 12. Composites of geopotential height anomalies (m) at 200hPa for the CFSv2 model, conditioned on the magnitude of the ENSO and IOD indices (see text). From top (left) to bottom (right) for IODs (ENSOs) classified as strong positive, moderate positive, neutral, moderate negative and strong negative.



265 The combination of El Niño events and positive IOD phase is associated with a more intense anomalous circulation pattern than that associated with pure El Niño events, either moderate or strong (Fig. 12, upper right panel). However, the combination of La Niña and negative IOD is not associated with a coherent change in the circulation anomalies (Fig. 12, lower left panel). Composites associated with moderate and strong negative IODs combined with a moderate La Niña events are not notably different from that for the pure moderate La Niña events. On the other hand, the combination of strong La Niña with moderate or strong IOD tends to amplify the anomalous circulation pattern over middle and high latitudes.

270 The SNR was also analyzed for the expanded set of composites. SNR is small (less than 0.5) for the moderate IOD events of both IOD phases and for the strong negative ones (Fig. 13 middle row). However, SNR for the strong positive IOD events exhibits larger values associated with the IO wave train. Although an intensification of circulation anomalies for all El Niño events along with positive IODs was found relative to those for pure El Niño (Fig. 12), SNR changes differ according to the intensity of the events (Fig. 13 upper right panel). For both moderate and strong El Niño events, SNR does not increase noticeably when they are combined with moderate positive IODs, which suggests that even though the circulation pattern intensifies, the noise does too. In contrast, when El Niño occurs simultaneously with strong positive IODs, the SNR increases throughout the entire domain, including the IO wave train. On the other hand, neither moderate nor strong events of negative IOD show substantial SNR changes when occurring concurrently with moderate La Niña. However, SNR increases at middle and high latitudes when strong La Niñas combine with negative IOD events. These results are consistent with the positive skewness in the DMI described in the reanalysis (section 3.1). Due to their higher intensity, the observed pure positive IOD events show a stronger signal than pure negative IODs.

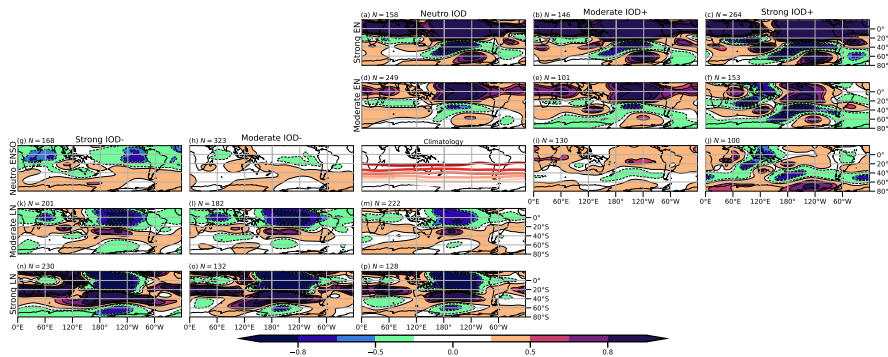


Figure 13. As Fig. 12 but for signal-to-noise ratio of geopotential height anomalies at 200hPa.

3.3 Temperature and precipitation

285 We evaluate the impact of the combined activity of ENSO and IOD on surface air temperature and precipitation in the major continental land masses south of 20°S. Following the same procedure as for the atmospheric circulation variables, Figure 14 shows the regression fields of temperature and precipitation anomalies in SON using the observational datasets described in



section 2. In addition, Figures 15 and 16 show the composites of temperature and precipitation anomalies, respectively. It is important to note that the regression still has the limitation of capturing only the linear aspect of the problem, and the composites are constrained by the number of samples available. Also, for pure IOD composites, it is worth keeping in mind that the observed negative events are less intense than the positive ones.

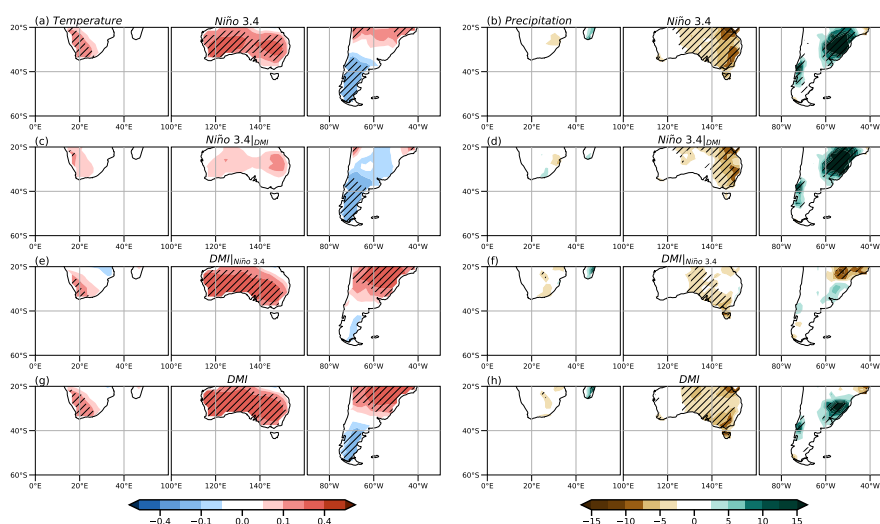


Figure 14. Regression of temperature from CRU dataset ($^{\circ}\text{C}$, left) and precipitation anomalies from GPCP dataset (mm, right) from top to bottom Niño 3.4, partial Niño 3.4, partial DMI and DMI in the period 1940-2020. The dotted areas indicate 95% statistical significance with a t-test.

The ENSO full regression shows in Africa positive temperature anomalies that are smaller and less significant when the IOD effect is removed (Fig. 14a and c, respectively). On the other hand, these anomalies remain significant in the full and partial IOD regressions (Fig. 14e and g, respectively). For precipitation, the regression fields in all cases (Fig. 14h and f, respectively) indicate negligible anomalies across the entire African region considered. Regarding the composites, significant temperature anomalies are only observed in this region during La Niña events (Fig. 15d), which is consistent with the regression results. Regardless of the significance, temperature composites show good correspondence with the temperature regressions in the simultaneous cases for both phases (Fig. 15e and f) and in negative IODs (Fig. 15d). On the other hand, precipitation anomalies composite are also negligible at the southern tip, which is consistent with the regressions.

In Australia, the full regression fields of temperature anomalies are similar for ENSO and IOD (Fig. 14a and g, respectively), with positive anomalies over most of the territory. However, the ENSO pattern of positive anomalies loses all its significance and intensity when the effect of the IOD is removed (Fig. 14c). On the contrary, the IOD-related anomalies maintain their significance even without considering ENSO (Fig. 14e). Therefore, the IOD seems to be more important in influencing temperature anomalies than ENSO. For precipitation, the full regression fields are similar for ENSO and IOD, with negative anomalies across the eastern half of the domain (Fig. 14b and h, respectively), which is consistent with Holgate et al. (2022). However,

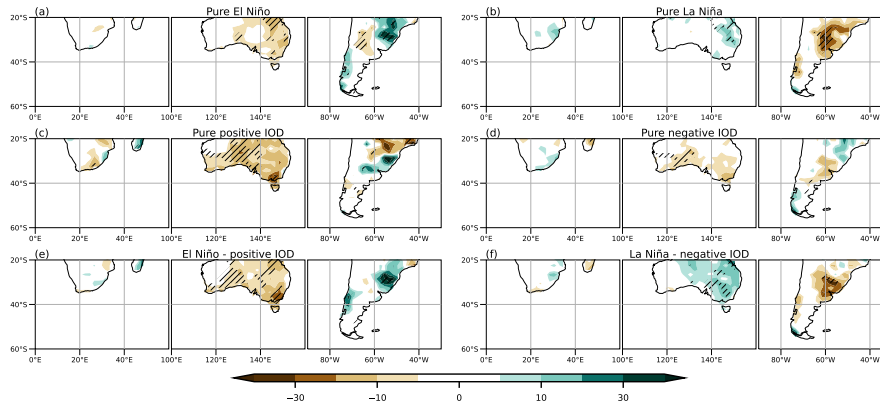


Figure 15. Composites of temperature anomalies from CRU dataset ($^{\circ}\text{C}$) for positive (left) and negative (right) events for ENSO (top), IOD (middle) and simultaneous ENSO-IOD (bottom) in the period 1940-2020. The dotted areas indicate 95% statistical significance with a Monte Carlo test (see text).

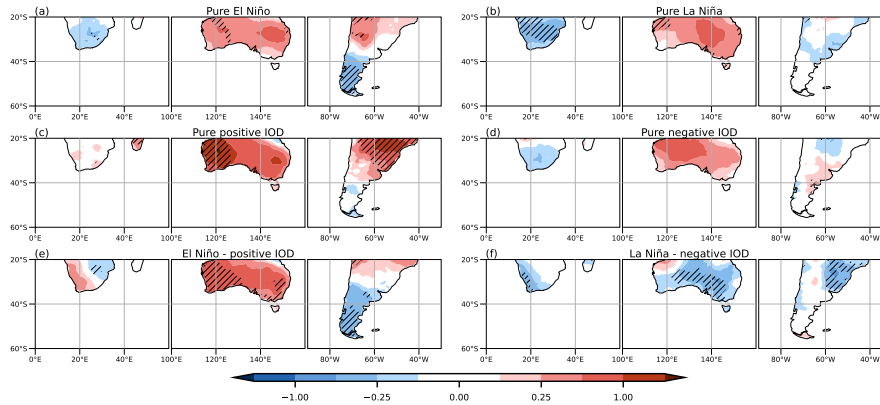


Figure 16. As Fig. 15 but for precipitation anomalies from GPCP dataset (mm).

305 the partial regression fields reveal that ENSO has more intense and focused influence in eastern Australia (Fig. 14d), while for IOD the anomalies are weaker and localized in the center-south (Fig. 14f). In the temperature anomaly composites, the positive IOD phase is consistent with the regression, although it does not have much significance (Fig. 15 a, c and e). On the other hand, La Niña and negative IOD composites show the same anomaly as in the positive phase and no significance (Fig. 15 b and d, respectively), i.e., the opposite of what can be assumed from the linear regression. Only in the simultaneous events (Fig. 15 e and f) does the behavior agree with what is described by the regression for both phases, although almost without significance.

310 In the precipitation anomaly composites, the behavior is similar to that for temperature. In composites for all positive phases (Fig. 16 a, c and e), significant precipitation anomalies align with the regression, but in negative phases, only La Niña and



the combination of La Niña with negative IOD exhibit this consistency (Fig. 16 b and f, respectively). For negative IOD, the anomalies are close to zero (Fig. 16d).

315 In South America, the full regression fields of temperature anomalies for ENSO and IOD are similar (Fig. 14 a and g, respectively), but they exhibit some differences that become evident in the partial regression. In the ENSO partial regression when the IOD is removed (Fig. 14 c), negative anomalies are observed at middle and high latitudes of this region, being more intense and significant in the southern tip of the continent, in agreement with previous results (Cai et al., 2020). On the other hand, in the IOD partial regression pattern (Fig. 14 e), positive temperature anomalies are observed in the center
320 of the continent, with anomalies close to zero in the further south, in agreement with Saji et al. (2005). For precipitation, the full regression fields over South America are similar in sign for ENSO and IOD (Fig. 14 b and h, respectively), but for the former they are much more intense. Moreover, when the IOD effect is removed from ENSO (Fig. 14 d), the pattern of anomalies remains almost the same, but the region of positive anomalies in the east central part of the continent shifts slightly northward as it intensifies. This ENSO-related precipitation anomaly pattern is in agreement with Cai et al. (2020). On the
325 other hand, when the ENSO effect is removed from the IOD (Fig. 14 f), a north-south dipole is observed in the east-central part of the continent that agrees in sign with Chan et al. (2008), but not in intensity. As in the other continents, composites of temperature anomalies agree with the regression in the positive phases but not in the negative ones (Fig. 15 left and right columns, respectively), where the intensity is also smaller. For precipitation, the anomaly composites (Fig. 16) align in terms of sign with the regression results for both phases. However, the agreement is more pronounced in intensity and significance
330 for the positive phases (Fig. 16, left column).

As for the circulation anomalies, the asymmetric intensity of the response between the positive and negative phases of the IOD, and its joint action with ENSO, is also observed in the precipitation and temperature effects over the three continents. Moreover, this asymmetry seems to depend on the variable and the combined activity or not of ENSO and IOD. All of this highlights the complexity and the need to understand how both large-scale variability patterns influence the austral spring
335 climate of each continent in more detail.

4 Discussion and Conclusions

Previous investigations of the extratropical circulation associated with the IOD and its interaction with ENSO have provided different and even contradictory results mainly due to their assumptions and methodologies. Many of these studies assumed symmetry in magnitude of the IOD response on the large-scale circulation (Saji and Yamagata, 2003a, b; Cai et al., 2011),
340 which was later refuted by Cai et al. (2012). However, Cai et al. (2012) employed linear regression without separating the effects of ENSO and IOD (for the large-scale circulation analysis) due to the high correlation between their indices in SON. This can lead to the observed characteristics not being uniquely attributable to each event (ENSO or IOD), especially during the positive phases of both IOD and ENSO, where the correlation is stronger than that of the negative phase. This limitation also arises when using partial regression but in the opposite direction, as attempting to isolate the effects may eliminate individual
345 characteristics. In our study, we complemented our analysis of the partial regression by employing composites, and the CFSv2



model outputs to provide a wider and more complex analysis of the separated and combined influence of both IOD and ENSO over the austral spring climate anomalies in the SH.

By comparing the results obtained with the three methodologies, it is evident that while the IOD positive phase is associated with significant anomalies in the circulation of the entire SH, IOD negative phase presents a less consistent anomaly circulation anomaly pattern. Compared to positive IODs, the response on SH circulation of negative IODs show higher inter-event variability, lower significance, and a lower magnitude. The same is found for temperature and precipitation anomalies on the three continents. These differences may be due to the magnitude of the events since, as it was shown in this study and in agreement with previous works (Cai et al., 2013), positive IODs are typically more intense than the negative ones. The results suggest that the differences in the magnitude of the convection anomaly at the equatorial IO between both IOD phases could explain the observed differences in atmospheric responses between IOD phases.

Regarding the interplay between ENSO and IOD, the non-linearity/asymmetry in the intensity of the response between both phases of the IOD also comes into play. All results obtained with both regressions and composites based on both reanalysis, and CFSv2 model outputs, point in that positive IOD can reinforce the El Niño circulation by the merging of the IO wave train with the PSA-like pattern over the Pacific Ocean. The CFSv2 model results also suggest that the co-occurrence of moderate positive IOD events with El Niño events does not result in a SNR increase. However, strong positive IODs can contribute to increasing the circulation signal of both moderate and strong El Niño circulation anomalies and the IO wave train. On the other hand, negative IOD in combination with La Niña does not have that clear joint influence on the circulation. There is a moderate intensification of the circulation associated with La Niña, accompanied by some changes in the location of the anomalous circulation centers. However, unlike El Niño and positive IOD, the results vary considerably between linear regression, the observed, and model composites. It is worth noting that, like for pure IOD, negative simultaneous events (La Niña–negative IOD) are less intense than positive ones. Moderate and strong negative IODs from the model simulation do not produce important changes in the intensity and SNR of the moderate La Niña circulation pattern. On the other hand, the combination of strong La Niña with moderate and strong IOD gives rise to the intensification of anomalies and the SNR of the circulation pattern at middle and high latitudes.

Finally, the influence of pure IOD and its combination with ENSO on precipitation and temperature over the three continents in midlatitudes is affected by the differences found between the IOD phases mentioned above. The magnitude and sign of the response associated with ENSO and IOD vary markedly depending on their phase and the variable to be considered. This is important for impact analysis of interest to productive sectors in extratropical regions where ENSO and IOD have influence, for example, on corn crops in Argentine Pampa region (Muller et al., 2015) and wheat crops in Australia (Yuan and Yamagata, 2015; Ummenhofer et al., 2009).

In conclusion, the IOD positive phase can have effects over the entire SH extratropical circulation and that can intensify in combination with El Niño. These results highlight the importance of considering the IOD when studying and characterizing ENSO events. On the other hand, negative IODs can modulate the circulation response to strong La Niñas, although the results exhibit considerable inter-event variability that requires further study.



380 *Code availability.* All codes used in this work can be found at <https://github.com/LucianoAndrian/ENSO-IOD>.

Data availability. Raw ERA5 reanalysis data can be found at <https://cds.climate.copernicus.eu>, CFSv2 model outputs at <http://iridl.ldeo.columbia.edu/SOURCES/Models/.NMME/>, CRU temperature at https://crudata.uea.ac.uk/cru/data/hrg/cru_ts_4.05/ and GPCC precipitation at <https://www.psl.noaa.gov/data/gridded/data.gpcc.html>

Author contributions. Luciano G. Andrian: data curation; formal analysis; investigation; methodology; visualization; writing – original draft.
385 Marisol Osman: conceptualization; data curation; supervision; methodology; writing. Carolina S. Vera: funding acquisition; project administration; resources; conceptualization; supervision; methodology; writing.

Competing interests. The authors declare that they have no conflict of interests that could have influenced the work reported in this paper.

Acknowledgements. The research was supported by UBACyT 20020220100075BA, PIP 11220200102038CO, PICT-2021-GRF-TI-00498 and the CLIMAX Project funded by Belmont Forum/ANR-15-JCL/-0002-01. LGA is supported by a fellowship grant from CONICET. We
390 acknowledge the agencies that support the NMME-Phase II system, and we thank the climate modeling groups (Environment Canada, NASA, NCAR, NOAA/GFDL, NOAA/NCEP, and University of Miami) for producing and making available their model output. NOAA/NCEP, NOAA/CTB, and NOAA/CPO jointly provided coordinating support and led development of the NMME-Phase II system. We thank the members of DiVar group of University of Buenos Aires-CONICET, Argentina for their valuable comments during the development of this research.



395 References

- Cai, W., Rensch, P., Cowan, T., and Hendon, H.: Teleconnection Pathways of ENSO and the IOD and the Mechanisms for Impacts on Australian Rainfall, *Journal of Climate - J CLIMATE*, 24, 3910–3923, <https://doi.org/10.1175/2011JCLI4129.1>, 2011.
- Cai, W., Rensch, P., Cowan, T., and Hendon, H.: An Asymmetry in the IOD and ENSO Teleconnection Pathway and Its Impact on Australian Climate, *Journal of Climate*, 25, 6318–6329, <https://doi.org/10.1175/JCLI-D-11-00501.1>, 2012.
- 400 Cai, W., Zheng, X.-T., Weller, E., Collins, M., Cowan, T., Lengaigne, M., Yu, W., and Yamagata, T.: Projected response of the Indian Ocean Dipole to greenhouse warming, *Nature Geoscience*, <https://doi.org/10.1038/ngeo2009>, 2013.
- Cai, W., McPhaden, M., Grimm, A., Rodrigues, R., Taschetto, A., Garreaud, R., Dewitte, B., Poveda, G., Ham, Y.-G., Santoso, A., Ng, B., Anderson, W., Wang, G., Geng, T., Jo, H.-S., Marengo, J., Alves, L., Osman, M., Li, S., and Vera, C.: Climate impacts of the El Niño–Southern Oscillation on South America, *Nature Reviews Earth Environment*, 1, 215–231, <https://doi.org/10.1038/s43017-020-0040-3>, 2020.
- 405 Chan, S., Behera, S., and Yamagata, T.: Indian Ocean Dipole influence on South American rainfall, *Geophysical Research Letters*, 35, <https://doi.org/10.1029/2008GL034204>, 2008.
- Fan, L., Liu, Q., Wang, C., and Guo, F.: Indian Ocean Dipole Modes Associated with Different Types of ENSO Development, *Journal of Climate*, 30, <https://doi.org/10.1175/JCLI-D-16-0426.1>, 2016.
- 410 Gillett, Z., Hendon, H., Arblaster, J., Lin, H., and Fuchs, D.: On the Dynamics of Indian Ocean Teleconnections into the Southern Hemisphere during Austral Winter, *Journal of the Atmospheric Sciences*, <https://doi.org/10.1175/JAS-D-21-0206.1>, 2022.
- Harris, I., Osborn, T., Jones, P., and Lister, D.: Version 4 of the CRU TS monthly high-resolution gridded multivariate climate dataset, *Scientific Data*, 7, <https://doi.org/10.1038/s41597-020-0453-3>, 2020.
- Hersbach, H., Bell, B., Berrisford, P., Hirahara, S., Horányi, A., Muñoz Sabater, J., Nicolas, J., Peubey, C., Radu, R., Schepers, D., Simmons, A., Soci, C., Abdalla, S., Abellan, X., Balsamo, G., Bechtold, P., Biavati, G., Bidlot, J., Bonavita, M., and Thépaut, J.-N.: The ERA5 global reanalysis, *Quarterly Journal of the Royal Meteorological Society*, <https://doi.org/10.1002/qj.3803>, 2020.
- 415 A., Soci, C., Abdalla, S., Abellan, X., Balsamo, G., Bechtold, P., Biavati, G., Bidlot, J., Bonavita, M., and Thépaut, J.-N.: The ERA5 global reanalysis, *Quarterly Journal of the Royal Meteorological Society*, <https://doi.org/10.1002/qj.3803>, 2020.
- Holgate, C., Evans, J. P., Taschetto, A. S., Gupta, A. S., and Santoso, A.: The Impact of Interacting Climate Modes on East Australian Precipitation Moisture Sources, *Journal of Climate*, 35, 3147 – 3159, <https://doi.org/10.1175/JCLI-D-21-0750.1>, 2022.
- Huang, B., Thorne, P. W., Banzon, V. F., Boyer, T., Chepurin, G., Lawrimore, J. H., Menne, M. J., Smith, T. M., Vose, R. S., and Zhang, H.-M.: Extended Reconstructed Sea Surface Temperature, Version 5 (ERSSTv5): Upgrades, Validations, and Intercomparisons, *Journal of Climate*, 30, 8179 – 8205, <https://doi.org/10.1175/JCLI-D-16-0836.1>, 2017.
- 420 H.-M.: Extended Reconstructed Sea Surface Temperature, Version 5 (ERSSTv5): Upgrades, Validations, and Intercomparisons, *Journal of Climate*, 30, 8179 – 8205, <https://doi.org/10.1175/JCLI-D-16-0836.1>, 2017.
- Karoly, D. J.: Southern Hemisphere Circulation Features Associated with El Niño–Southern Oscillation Events, *Journal of Climate*, 2, 1239 – 1252, [https://doi.org/10.1175/1520-0442\(1989\)002<1239:SHCFAW>2.0.CO;2](https://doi.org/10.1175/1520-0442(1989)002<1239:SHCFAW>2.0.CO;2), 1989.
- Kiladis, G. N.: Observations of Rossby Waves Linked to Convection over the Eastern Tropical Pacific, *Journal of the Atmospheric Sciences*, 55, 321 – 339, [https://doi.org/10.1175/1520-0469\(1998\)055<0321:OORWLT>2.0.CO;2](https://doi.org/10.1175/1520-0469(1998)055<0321:OORWLT>2.0.CO;2), 1998.
- 425 55, 321 – 339, [https://doi.org/10.1175/1520-0469\(1998\)055<0321:OORWLT>2.0.CO;2](https://doi.org/10.1175/1520-0469(1998)055<0321:OORWLT>2.0.CO;2), 1998.
- Kumar, A. and Chen, M.: What is the variability in US west coast winter precipitation during strong El Niño events?, *Climate Dynamics*, 49, 1–14, <https://doi.org/10.1007/s00382-016-3485-9>, 2017.
- Kumar, A., Chen, M., Zhang, L., Wang, W., Xue, Y., Wen, C., Marx, L., and Huang, B.: An Analysis of the Nonstationarity in the Bias of Sea Surface Temperature Forecasts for the NCEP Climate Forecast System (CFS) Version 2, *Monthly Weather Review*, 140, 3003 – 3016, <https://doi.org/10.1175/MWR-D-11-00335.1>, 2012.
- 430 <https://doi.org/10.1175/MWR-D-11-00335.1>, 2012.



- Mo, K.: Relationships between Low-Frequency Variability in the Southern Hemisphere and Sea Surface Temperature Anomalies, *Journal of Climate*, 13, [https://doi.org/10.1175/1520-0442\(2000\)013<3599:RBLFVI>2.0.CO;2](https://doi.org/10.1175/1520-0442(2000)013<3599:RBLFVI>2.0.CO;2), 2000.
- Muller, G. V., Fernández Long, M. E., and Bosch, E.: Relación entre la temperatura de la superficie del mar de diferentes océanos y los rendimientos de maíz en la Pampa Húmeda, *Meteorológica*, 40, 5–16, 2015.
- 435 Osman, M. and Vera, C.: Climate predictability and prediction skill on seasonal time scales over South America from CHFP models, *Climate Dynamics*, 49, 2365–2383, <https://doi.org/10.1007/s00382-016-3444-5>, 2017.
- Saha, S., Moorthi, S., Wu, X., Wang, J., Nadiga, S., Tripp, P., Behringer, D., Hou, Y.-T., Chuang, H.-Y., Iredell, M., Ek, M., Meng, J., Yang, R., Peña, M., Dool, H., Zhang, Q., Wang, W., Chen, M., and Becker, E.: The NCEP climate forecast system version 2, *Journal of Climate*, 27, 2185–2208, <https://doi.org/10.1175/JCLI-D-12-00823.1>, 2014.
- 440 Saji, H. and Yamagata, T.: Structure of SST and Surface Wind Variability during Indian Ocean Dipole Mode Events: COADS Observations*, *Journal of Climate*, 16, 2735–2751, [https://doi.org/10.1175/1520-0442\(2003\)016<2735:SOSASW>2.0.CO;2](https://doi.org/10.1175/1520-0442(2003)016<2735:SOSASW>2.0.CO;2), 2003a.
- Saji, H. and Yamagata, T.: Possible impacts of Indian Ocean Dipole Mode events on global climate, *Climate Research - CLIMATE RES*, 25, 151–169, <https://doi.org/10.3354/cr025151>, 2003b.
- Saji, H., Goswami, B. N., Vinayachandran, P., and Yamagata, T.: A dipole mode in the Tropical Indian Ocean, *Nature*, 401, 360–3, <https://doi.org/10.1038/43854>, 1999.
- 445 Saji, H., Ambrizzi, T., and Ferraz, S.: Indian Ocean Dipole mode events and austral surface air temperature anomalies, *Dynamics of Atmospheres and Oceans - DYNAM ATMOS OCEANS*, 39, 87–101, <https://doi.org/10.1016/j.dynatmoce.2004.10.015>, 2005.
- Schneider, U., Becker, A., Finger, P., Rustemeier, E., and Ziese, M.: GPCP Full Data Monthly Version 2020 at 0.25°: Monthly Land-Surface Precipitation from Rain-Gauges built on GTS-based and Historic Data, https://doi.org/10.5676/DWD_GPCP/FD_M_V2020_025, 2020.
- 450 Sena, A. C. T. and Magnusdottir, G.: Influence of the Indian Ocean Dipole on the Large-Scale Circulation in South America, *Journal of Climate*, 34, 6057 – 6068, <https://doi.org/https://doi.org/10.1175/JCLI-D-20-0669.1>, 2021.
- Stuecker, M. F., Timmermann, A., Jin, F.-F., Chikamoto, Y., Zhang, W., Wittenberg, A. T., Widiasih, E., and Zhao, S.: Revisiting ENSO/Indian Ocean Dipole phase relationships, *Geophysical Research Letters*, 44, 2481–2492, <https://doi.org/https://doi.org/10.1002/2016GL072308>, 2017.
- 455 Sun, S., Lan, J., Fang, Y., Tana, C., and Gao, X.: A Triggering Mechanism for the Indian Ocean Dipoles Independent of ENSO, *Journal of Climate*, 28, 5063–5076, <https://doi.org/10.1175/JCLI-D-14-00580.1>, 2015.
- Takaya, K. and Nakamura, H.: A Formulation of a Phase-Independent Wave-Activity Flux for Stationary and Migratory Quasigeostrophic Eddies on a Zonally Varying Basic Flow, *Journal of The Atmospheric Sciences - J ATMOS SCI*, 58, 608–627, [https://doi.org/10.1175/1520-0469\(2001\)058<0608:AFOAPI>2.0.CO;2](https://doi.org/10.1175/1520-0469(2001)058<0608:AFOAPI>2.0.CO;2), 2001.
- 460 Ummenhofer, C., England, M., McIntosh, P., Meyers, G., Pook, M., Risbey, J., Sen Gupta, A., and Taschetto, A.: What causes Southeast Australia’s worst droughts?, *Geophysical Research Letters - GEOPHYS RES LETT*, 36, <https://doi.org/10.1029/2008GL036801>, 2009.
- Vinayachandran, P., Pavanathara, F., and Rao, S.: Indian Ocean dipole: processes and impacts, *Current Trends in Science*, 2010.
- Wang, H., Kumar, A., Murtugudde, R., Narapusetty, B., and Seip, K.: Covariations between the Indian Ocean dipole and ENSO: a modeling study, *Climate Dynamics*, 53, <https://doi.org/10.1007/s00382-019-04895-x>, 2019.
- 465 Yuan, C. and Yamagata, T.: Impacts of IOD, ENSO and ENSO Modoki on the Australian Winter Wheat Yields in Recent Decades, *Scientific Reports*, 5, 17 252, <https://doi.org/10.1038/srep17252>, 2015.
- Zhao, S., Jin, F., and Stuecker, M.: Improved Predictability of the Indian Ocean Dipole Using Seasonally Modulated ENSO Forcing Forecasts, *Geophysical Research Letters*, 46, 9980–9990, <https://doi.org/10.1029/2019GL084196>, 2019.